Supplementary Material: Exploiting high-slip flow regimes to improve inference of glacier bed topography

Alexi Morin[1]*, Gwenn E. Flowers[1], Andrew Nolan[1], Douglas Brinkerhoff[2], Etienne Berthier[3]

[1]*Department of Earth Sciences, Simon Fraser University, Burnaby, British Columbia, Canada*

[2]*Department of Computer Science, University of Montana, Missoula, Montana, USA*

[3]*LEGOS, Université de Toulouse, CNES, CNRS, IRD, UPS, 31400 Toulouse, France*

1 BAYESIAN INFERENCE APPROACH

1.1 Gaussian processes

Figure S1 graphically defines hyper-parameters σ (amplitude) and ℓ (correlation lengthscale) and illustrates the sensitivity of a Gaussian process to observations.

1.2 Metropolis–Hastings Algorithm

The posterior distributions of the variables have no closed form (Gelman and others, 1995), thus necessitating that we approximate them. Following Brinkerhoff and others (2016) we do this using the Metropolis–Hastings Algorithm implemented through the `python` library `pymc2` (Fonnesbeck and others, 2015). This algorithm determines how steps are taken in parameter space. After a sufficient number of steps, the sampled distribution is considered a subset of the true posterior distribution.

1.3 Defining hyper-parameters and model priors

Hyper-parameter values (Table S1) are chosen to be realistic and representative of the study glacier, with these choices guided by real observational uncertainties. Due to inconsistencies between variables in the case of the real data, adjustment of the priors, in the form of increasing the observational variance, was necessary in order to achieve realistic results. For example, the prescribed variance of the surface-elevation change rate ($\nu_{\frac{\Delta S}{\Delta t}}$) which exceeds observational uncertainty is used to minimize unrealistic inversion results

*Present address: Institut National de la Recherche Scientifique, Quebec City, Quebec, Canada

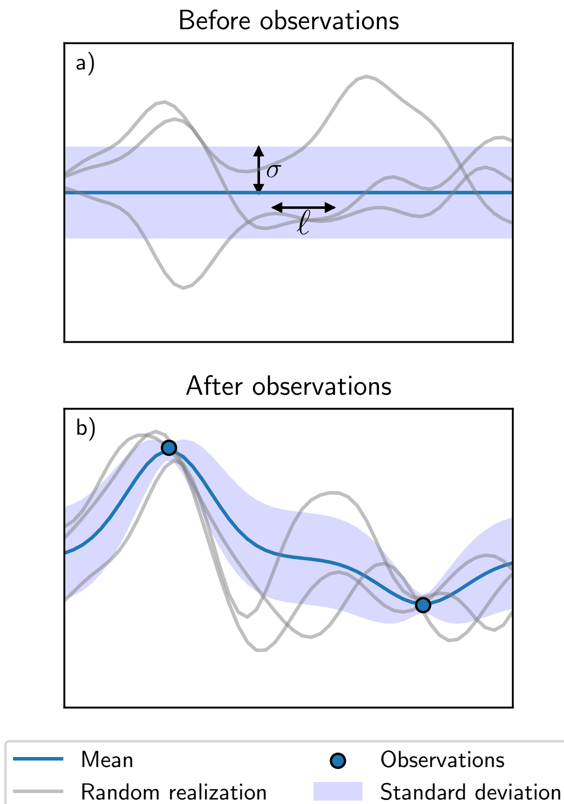

Fig. S1. Example of a Gaussian process and the influence of hyper-parameters. a) σ and ℓ influence random realisations of the Gaussian process. (b) The mean and covariance of the Gaussian process are influenced by observations.

Table S1. Hyper-parameters used in Bayesian inversion of real and synthetic data

Symbol	Value	Units	Description
σ_B	250	m	Bed-elevation amplitude
ν_B	25	m^2	Variance, observed bed elevation
ℓ_B	1000	m	Bed correlation lengthscale
σ_S	10	m	Surface-elevation amplitude
ν_S	100	m^2	Variance, observed surface elevation
$\sigma_{\dot{b}}$	10	$\mathrm{m\,a^{-1}}$	Mass-balance amplitude
$\nu_{\dot{b}}$	100	$\mathrm{m^2\,a^{-2}}$	Variance, observed mass balance
$\sigma_{\frac{\Delta S}{\Delta t}}$	10	$\mathrm{m\,a^{-1}}$	Surface-elevation change-rate amplitude
$\nu_{\frac{\Delta S}{\Delta t}}$	100	$\mathrm{m^2\,a^{-2}}$	Variance, observed surface-elevation change rate
ℓ	3000	m	Correlation lengthscale
ν_{U_s}	50	$\mathrm{m^2\,a^{-2}}$	Variance, observed surface velocities

in the vicinity of the glacier terminus. The same hyper-parameter values are applied to inversions of real and synthetic data.

The mean functions used to define the priors are as follows. Elevation change rate and ice thickness are taken as zero, with a positivity constraint on ice thickness. Flowband width is taken as uniform and equal to 0.5, while mass balance is prescribed to decline monotonically with flowline position on the basis of model output from Young and others (2021). Coefficient s is uniform across the domain, with the prior distribution defined as a truncated normal with lower and upper bounds of 1 and 1.25, respectively, a mean of 1 and standard deviation of 0.05. Prescribing a uniform rather than normal prior for s, as described in Brinkerhoff and others (2016), produced systematic biases in some inversions.

1.4 Assessing model convergence

Convergence is illustrated in Figure S2 with histograms of the Monte Carlo Markov Chains for two example bed posteriors. We compute at least three chains for every inversion, with at least 10^6 iterations, a burn-in period of 10^5 and a thinning factor of 10. We have found 10^6 iterations sufficient to obtain convergence in most cases, while the burn-in period and thinning factor were chosen to be conservative.

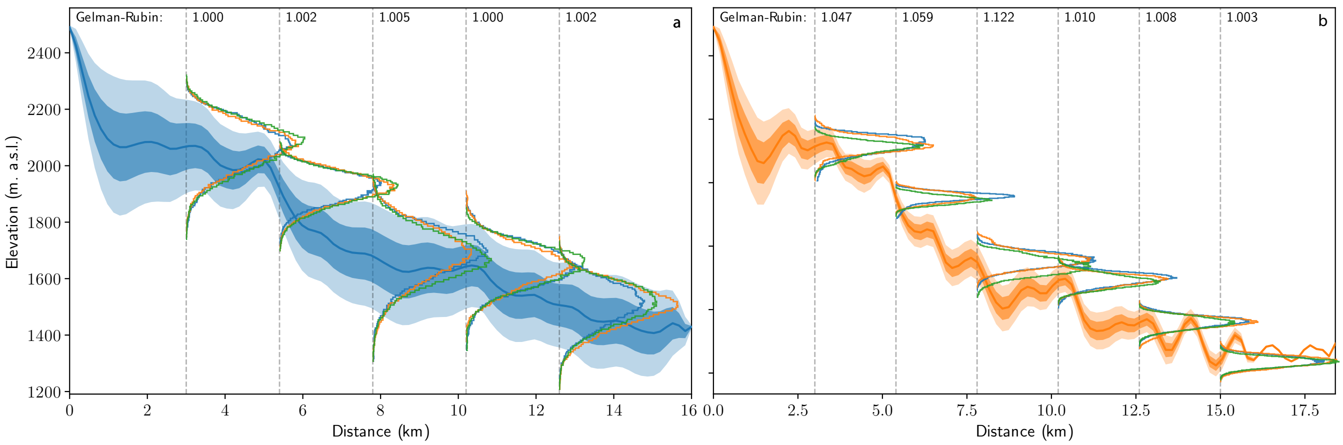

Fig. S2. Illustration of trace convergence, with histograms of the bed posterior shown for three traces at several locations along the flowline. Histograms should be normal, and similar between traces at any given location. Corresponding Gelman–Rubin statistics are shown at top. (a) Example synthetic bed posterior for inversion of data from deformation-only (quiescent) regime. (b) Example synthetic bed posterior for inversion of data from high-slip (surge) regime.

2 GENERATION OF SYNTHETIC DATA

2.1 Reference glacier geometry

The synthetic glacier geometry is derived from the site of interest in order for the synthetic results to be as instructive as possible. We begin by manually delineating an approximate flowline following the tributary involved in the 2018–2019 surge (Figure 1 in main text). We use the 30 m SRTM (Farr and others, 2007) Digital Elevation Model (DEM) contoured at 50 m for the purpose of delineating the flowline orthogonal to glacier surface contours. Our resulting flowline follows an OGGM generated flowline, without the abrupt changes in direction present in the OGGM (Maussion and others, 2019). We then extract glacier surface and bed profiles along the flowline at 10 m intervals. The surface elevations come from the 30 m SRTM DEM, while bed elevations are based on the dataset of Farinotti and others (2019) (hereafter referred to as “F2019”) (Figure S3a). We smooth the surface and bed profiles with a fifth-order Savgol filter from the `signal` subpackage from `scipy` using a using a window of 211 points or 2110 m (Figure S3b).

The F2019 ice-thickness model has systematic errors at the study location due, at least in part, to outdated glacier outlines. We attempt to manually correct these errors to create an accurate and stable synthetic reference geometry. Farinotti and others (2019) use the Randolph Glacier Inventory (RGI) version 6.0 outline (Consortium, 2017), which, in this case, includes the glacier of interest (dubbed “Little

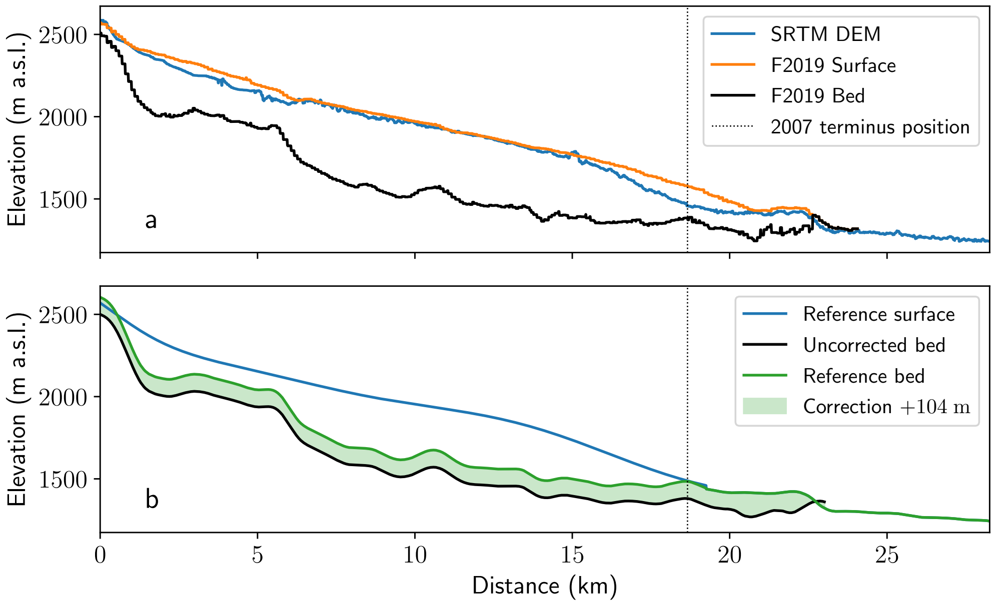

Fig. S3. Generation of synthetic glacier geometry. (a) Raw topographic profiles extracted along flowline (Figure 1, main text) at 10 m intervals from 30 m SRTM DEM (blue) and Farinotti and others (2019) (F2019) dataset (orange and black). (b) Smoothed and corrected profiles. Upstream end of flowline is truncated where bed elevation exceeds surface elevation after applying the correction. 2007 (pre-surge) terminus position is shown as dashed vertical line.

Kluane" in air photographs by Austin Post) as a tributary connected to the Kluane Glacier (RGI Glacier ID: 01.16198). This tributary, however, has retreated ∼3 km from its former confluence with the Kluane Glacier, meaning ice thickness is non-zero in the F2019 dataset over several kilometres of currently ice-free terrain.

The mean ice thickness estimated by Farinotti and others (2019) in this ice-free region is 104 m. We make a crude correction to the reference glacier geometry by increasing the F2019 bed elevation everywhere by 104 m. We truncate the uppermost portion of the flowline by ∼1 km, where bed elevation exceeds surface elevation after applying the correction (Figure S3b). Hereafter, we refer to the smoothed and corrected profiles (Figure S3b) as the "reference" profiles. The synthetic beds used in the ice-flow model (below) are the sum of the reference bed and various sinusoidal perturbations, as described in the main text.

2.2 Ice-flow model

We use the open-source finite-element model Elmer/Ice (Gagliardini and others, 2013) to generate synthetic glacier profiles, and associated surface elevations, elevation change rates and velocities, for different glacier beds. We solve the Stokes equations in two (x–z flowband) dimensions for incompressible flow:

$$\nabla \cdot \boldsymbol{\sigma} + \rho \boldsymbol{g} = 0 \tag{1}$$

$$\nabla \cdot \boldsymbol{u} = 0, \tag{2}$$

where ρ is ice density, $\boldsymbol{g}$ gravitational acceleration, $\boldsymbol{u}$ the ice velocity vector, and $\boldsymbol{\sigma} = \boldsymbol{\tau} - p\,\mathrm{I}$ the Cauchy stress tensor with deviatoric stress tensor $\boldsymbol{\tau}$, isotropic pressure p and identity matrix I. To close the system of equations above we use the Glen–Nye-type constitutive law for temperate ice

$$\boldsymbol{\tau} = A^{-1/n}\,\dot{\varepsilon}_{\mathrm{e}}^{(1-n)/n}\,\dot{\boldsymbol{\varepsilon}}, \tag{3}$$

where A is the rate factor, $\dot{\varepsilon}_{\mathrm{e}}$ the effective strain rate, $\dot{\boldsymbol{\varepsilon}}$ the strain rate tensor and $n = 3$ the stress exponent. Effects of variable flowband width and lateral drag are neglected. We assume a stress-free surface boundary such that

$$\boldsymbol{\sigma} \cdot \boldsymbol{n} = 0, \tag{4}$$

where $\boldsymbol{n}$ is unit vector normal to the boundary. The basal boundary condition is expressed as a linear friction law

$$\boldsymbol{\tau}_{\mathrm{b}} = \beta\,\boldsymbol{u}_{\mathrm{b}}, \tag{5}$$

where $\boldsymbol{\tau}_{\mathrm{b}}$ is basal shear stress, β the slip coefficient and $\boldsymbol{u}_{\mathrm{b}}$ the sliding speed (Gagliardini and others, 2013). All simulations are prognostic, meaning the free surface evolves according to

$$\frac{\partial z_{\mathrm{s}}}{\partial t} + u_{\mathrm{s}}\frac{\partial z_{\mathrm{s}}}{\partial x} - w_{\mathrm{s}} = \dot{b}, \tag{6}$$

where z_{s} is surface elevation, $\boldsymbol{u}_{\mathrm{s}} = (u_{\mathrm{s}}, w_{\mathrm{s}})$ are the horizontal and vertical surface velocities, respectively, obtained from the Stokes equations (1 and 2) and $\dot{b}$ is the surface mass balance described below. We assume rigid, impenetrable bedrock of elevation $z_{\mathrm{b}}(x)$, thus Equation 6 must satisfy the inequality

$$z_{\mathrm{s}}(x,t) \geqslant z_{\mathrm{b}}(x) + h_{\mathrm{min}}, \tag{7}$$

where h_{min} is a small non-zero ice thickness (10 m in this case) added to ice-free gridcells to facilitate the numerical treatment of this free-boundary problem (Gagliardini and others, 2013). Equations 1, 2 and 6

	Description	Value	Units
g	Gravitational acceleration	9.8	$\mathrm{m\,s^{-2}}$
ρ	Ice density	910	$\mathrm{kg\,m^{-3}}$
n	Stress (Glen) exponent	3	–
A	Rate Factor	5.016×10^{-24}	$\mathrm{Pa^{-3}\,s^{-1}}$

Table S2. Physical constants and fixed model parameters used in Elmer/Ice simulations.

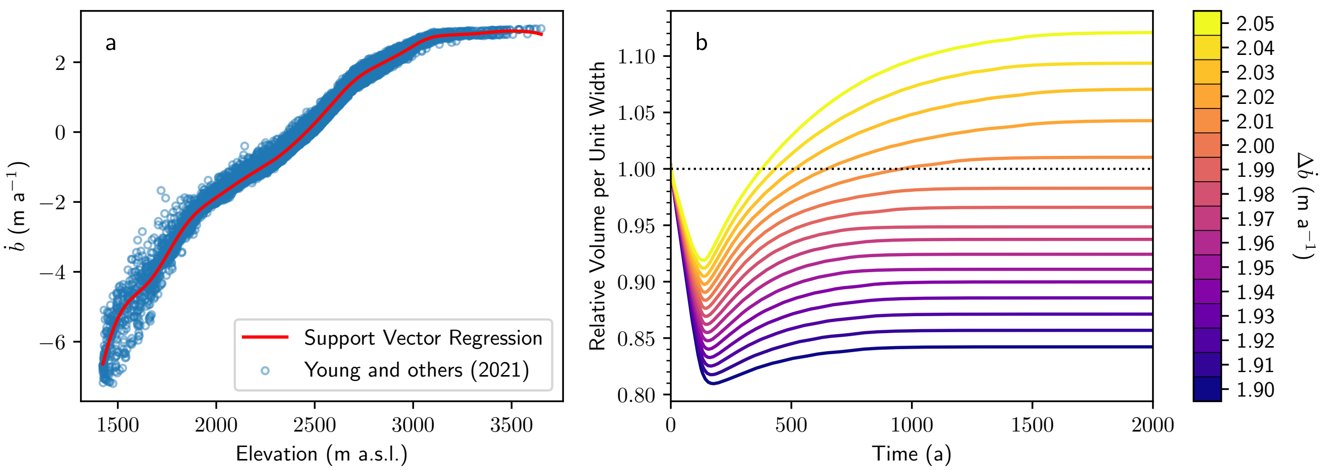

Fig. S4. Surface mass balance of the real and synthetic study glaciers. (a) Mass balance as a function of elevation as estimated using the model of Young and others (2021) (dots) with trained support vector regression (red line) used to prescribe the surface mass balance for the ice-flow model. (b) Relative glacier volume per unit width for the reference geometry over a 2 ka model spin-up for various offsets (colour) applied to the mass-balance–elevation profile in (a). Values in $\mathrm{m\,a^{-1}}$ ice-equivalent. An offset of $2.01\,\mathrm{m\,a^{-1}}$ ice-equivalent produces the steady-state closest to unity in this case.

are solved on a rectangular mesh with 10 vertical layers and a horizontal grid spacing of 50 m.

2.3 Surface mass balance

We use the mass-balance model of Young and others (2021), developed for the nearby Kaskawulsh Glacier (roughly 30 km from the study glacier), to estimate the surface mass balance across the glacier of interest and its synthetic counterpart. This model uses downscaled and bias-corrected air temperatures and precipitation from the North American Regional Reanalysis (NARR) dataset to estimate accumulation with a prescribed rain-to-snow threshold of 1°C, and calculates ablation with the enhanced temperature-index model of Hock (1999) and a refreezing parameterization. The temperature-index model parameters are tuned for the Kaskawulsh Glacier using the glacier-wide 2007–2018 geodetic balance, the average equilibrium line altitude (ELA) and in-situ surface mass-balance data. The geodetic balance of the Kaskawulsh Glacier has been indistinguishable from the regional average over several decades (Berthier and others, 2010), suggesting that this glacier may be regionally representative. We therefore use the model parameters tuned for the Kaskawulsh Glacier to simulate the surface mass balance of the glacier of interest from 2007–2018 (blue dots, Figure S4a).

We train a Support Vector Regression (SVR) with a radial basis kernel function using the 2007–2018 mean mass balance as a function of elevation with the `scikit-learn python` package (Pedregosa and others, 2011, Figure S4a). SVR is an extension of support vector classification that uses only a subset of the training data (i.e., the support vectors) to fit the model. A trained SVR model produces support vectors, dual coefficients (i.e., weights) and an intercept, which are used for prediction. Since Elmer/Ice boundary conditions must be prescribed in a `FORTRAN` function, we write the support vectors and weights to disk and do not use the `scikit-learn` application program interface. Prediction with the trained SVR model is done according to:

$$\hat{y}(x) = \sum_{i \in SV} (\alpha_i - \alpha_i^*) K(x, x_i) + b, \tag{8}$$

where $\hat{y}(x)$ is the predicted variable, SV are the support vectors, $\alpha_i - \alpha_i^*$ are the dual coefficients (i.e., weights), b is the intercept, and K is the radial basis kernel function of the form

$$K = \exp(-\gamma \|x - x_i\|^2), \tag{9}$$

where x is vector of positions where predictions are needed, x_i is the i^{th} support vector, and γ controls the influence of a single training sample. Optimal values for the hyperparameters C (an inverse regularization parameter) and γ were determined by cross validation.

2.4 Steady-state simulations

To produce self-consistent synthetic datasets that represent deformation-dominated (quiescent-like) glacier-flow regimes, we first compute steady states for each bed shown in Figure 4.1. Because the glacier of interest was not in steady state from 2007–2018, the prescribed mass-balance profile (Figure S4a) does not produce a glacier of similar size to the observed. We therefore run a suite of simulations, driven by incremental mass-balance offsets, for each glacier bed to obtain steady-state glaciers of similar size to the observed.

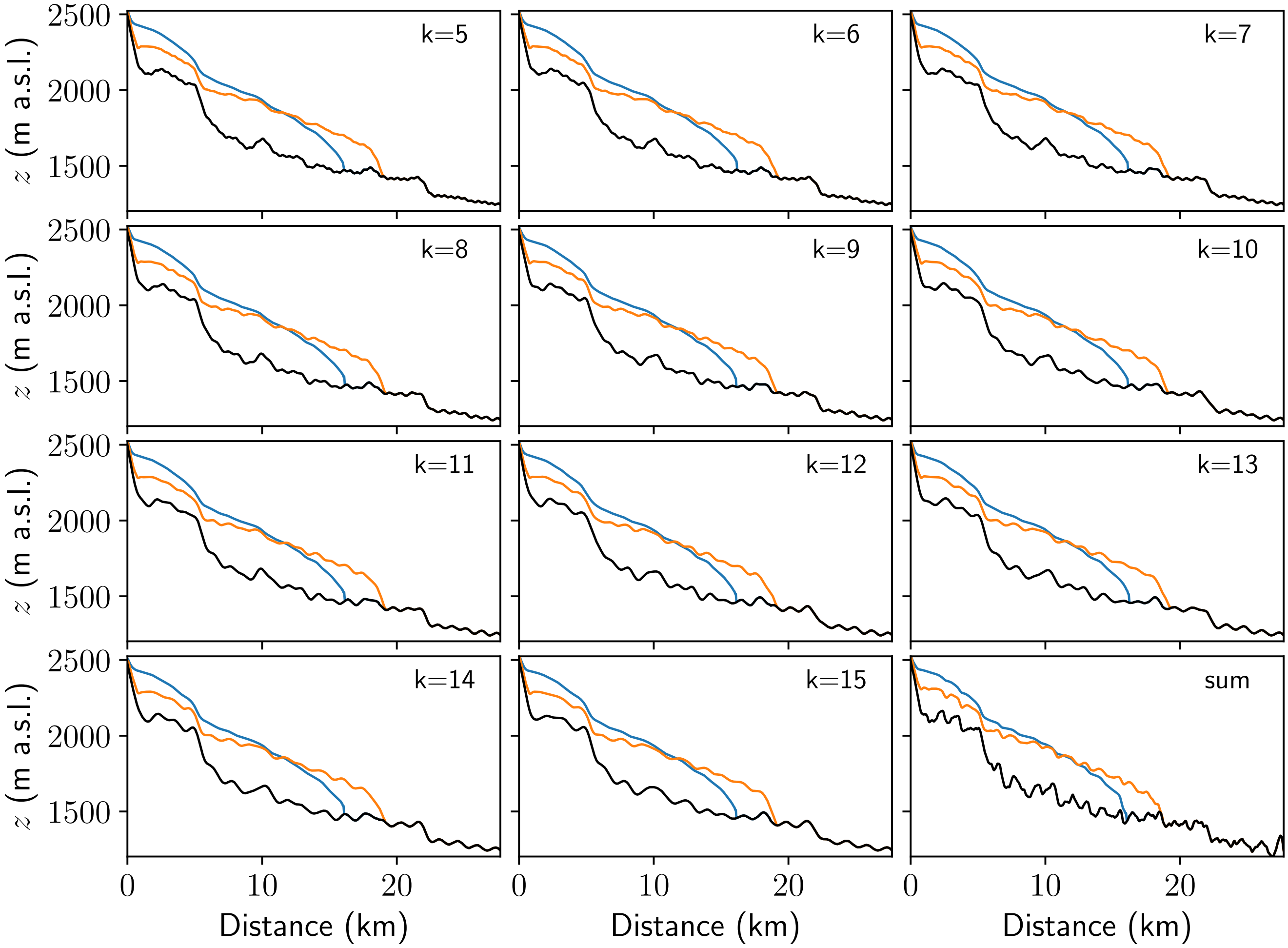

Fig. S5. Synthetic glacier geometries for each bed profile (see main text). Steady-state glacier surface profiles intended to represent quiescent flow regimes are shown in blue. Transient glacier surface profiles after 10 a of high sliding intended to represent surge-like flow are shown in orange.

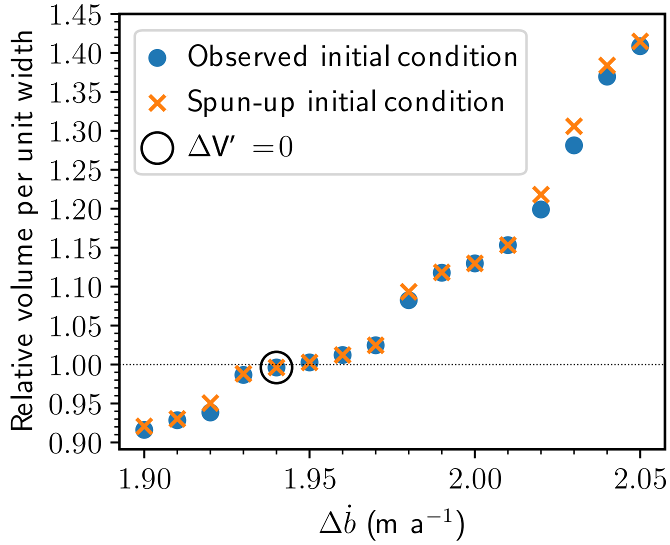

Fig. S6. Relative glacier volume per unit width for the composite bed (B_{synth} in main text) at the end of a 2 ka model spin-up as a function of offsets applied to the mass-balance profile. Results for both initial conditions are shown: (1) the observed reference profile (blue dots) and (2) the steady-state glacier profile (orange crosses). The mass-balance offset ($1.94\,\mathrm{m\,a^{-1}}$) t hat produces the steady-state glacier, for both initial conditions, is circled in black.

The reference geometry is initialized with the ice-surface topography shown in Figure S3b. We then use the resulting steady-state glacier profile for the reference geometry as the initial condition for each of the perturbed beds (see section below for more detail). All steady-state simulations are run with no sliding ($\beta = 1$ in sliding law, see main text). We test mass-balance offsets ranging from 1.90–2.05 $\mathrm{m\,a^{-1}}$ in increments of 0.01 $\mathrm{m\,a^{-1}}$. We run all simulations for 2 ka and compute the relative glacier volume per unit width (V') as:

$$V'(t) = \frac{\sum_{j=1}^{\mathrm{M}} H(x_j, t)\ \Delta x}{\sum_{j=1}^{\mathrm{M}} H(x_j, 0)\ \Delta x}, \tag{10}$$

where H is the ice thickness at position x_j and time t, M is the number of horizontal gridcells in the model domain and Δx is the horizontal gridcell spacing. The fictitious ice (of thickness $h_{\min}$) mentioned in ice-flow model description is removed in the calculation of relative volume per unit width. For each glacier bed, we define the steady-state configuration as the result of the simulation that produces V' closest to unity. The steady-state glacier profiles for each bed (Figure 4.1), and their associated surface velocities, are used to represent quiescent flow regimes in the inversions of synthetic data.

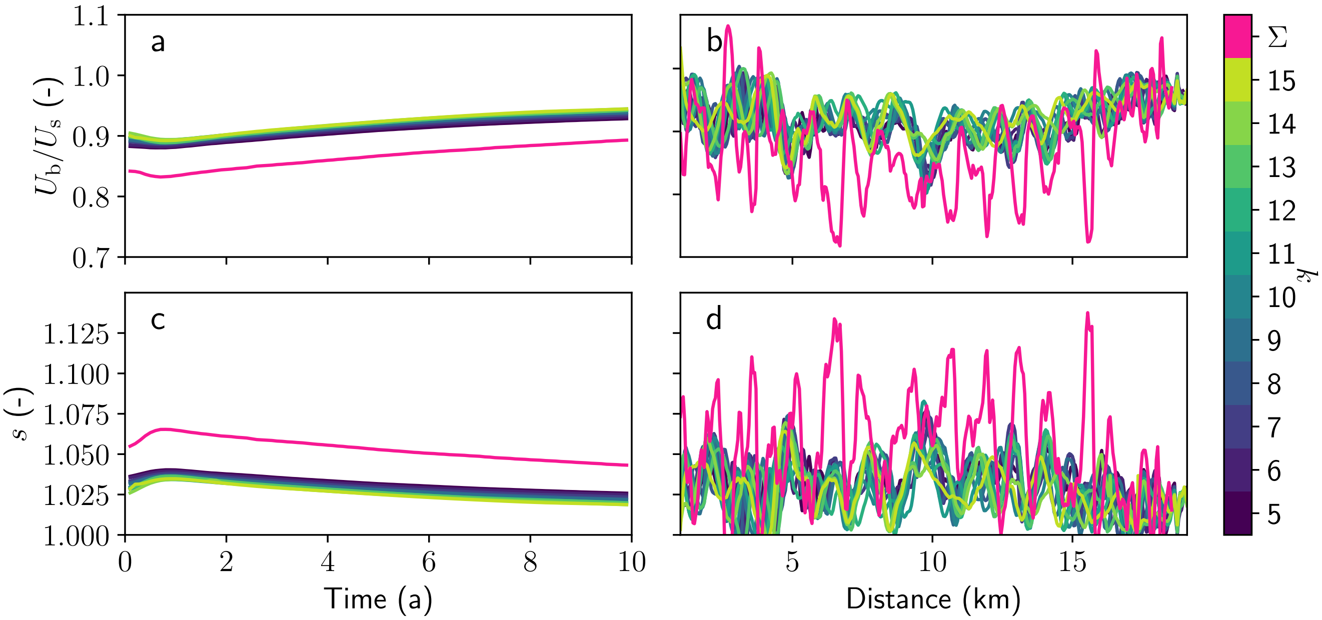

Fig. S7. Flow-regime diagnostics for transient high-slip simuations. (a), (b) Contribution of basal slip (U_b) to overall surface motion (U_s) expressed as a fraction, over time in (a) and distance in (b) for each bed (in colour). (c), (d) Value of s, as defined by Brinkerhoff and others (2016), over time in (c) and distance in (d) for each bed (in colour). Fuscia is the composite bed.

2.4.1 Initial conditions

For the perturbed bed steady-state simulations two natural choices arise for the initial condition: (1) the reference profile in Figure S3b based on observations or (2) the steady-state glacier profile that uses the reference profile as an initial condition. Figure S4b demonstrates a strong transient response, associated with the relaxation of the free-surface, during the first 500 a of a spin-up simulation initialized with (1). Using (2) instead avoids the free-surface relaxation, leading to shorter model run times required to achieve steady state: simulations using (2) reach steady state (defined as $|dV'/dt| \leqslant 10^{-7}$) 40% faster than simulations using (1). Despite the shorter run times with (2), the final relative volume per unit width (V') differs by an average of 0.5 % and a maximum of 1.9 % compared to simulations using (1) (Figure S6). We therefore initialize spin-up simulations for the perturbed beds using (2).

2.5 Emulation of surging flow

To produce synthetic datasets that represent slip-dominated glacier-flow regimes, and therefore mimic glacier surges, we perturb the coefficient β in the sliding law. For each glacier bed we use the corresponding steady-state surface profile (blue lines in Figure 4.1) described above as the initial condition. We prescribe a uniform slip coefficient $\beta = 3.5 \times 10^{-4}\,\mathrm{MPa\,a\,m^{-1}}$ over the entire model domain except the glacier headwall ($x \leqslant 2\,\mathrm{km}$). This value of β was determined by trial and error to produce an amount of terminus advance similar to that associated with the 2018–2019 surge of the real glacier. The slip-dominated simulations are run for 10 a, with a time-step of 0.1 a to ensure numerical stability. The resulting surface profiles at the end of the 10 a simulations are shown as orange lines in Figure 4.1.

Back-calculated values of the contribution of basal slip to surface motion in these simulations demonstrate the slip-dominated nature of these flow regimes (Figures S7a,b), with all values above 0.8. The least slip-dominated regime is that of the composite bed (fuscia in Figure S7) owing to its comparatively high roughness (see Figure 4.1). Back-calculated values of the coefficient s as defined by Brinkerhoff and others (2016) are also shown (Figures S7c,d). This quantity relates depth-averaged velocity $\bar{U}(r)$ to surface velocity $U_s(r) = s\,\bar{U}(r)$, such that $s = 1$ corresponds to pure sliding (plug flow) and $s = (n+2)/(n+1) = 1.25$ corresponds to pure deformation under idealized conditions (Nye, 1965).

3 DISTRIBUTIONS OF MODEL VARIABLES FOR SYNTHETIC DATA

Figure S8 shows distributions of surface speed, elevation change rate, mass balance and surface/bed elevation for all four inversions of synthetic data for the composite glacier bed.

4 ADDITIONAL INVERSIONS WITH SYNTHETIC DATA

4.1 Inversions of synthetic data for beds defined by individual values of k

Figures S9–S12 show the results of inversions of synthetic data for beds defined by individual values of k along with the composite bed (see Figure 4.1), while Figure shows the prior and posterior distributions of s for each of these simulations. Figure S14 summarizes performance metrics between the true and inferred beds for all four inversions. Values of r and RMSE in Figure S14 represent the mean values of distributions generated by computing r and RMSE between the true bed and all realizations of the bed in the posterior distributions. These metrics therefore comprise a comparison with the full posterior distributions of the bed.

The mean correlation coefficient r (Figure S14a) generally increases with k for all four inversions, illustrating the greater ease with which longer-wavelength bed topography can be recovered. For nearly all

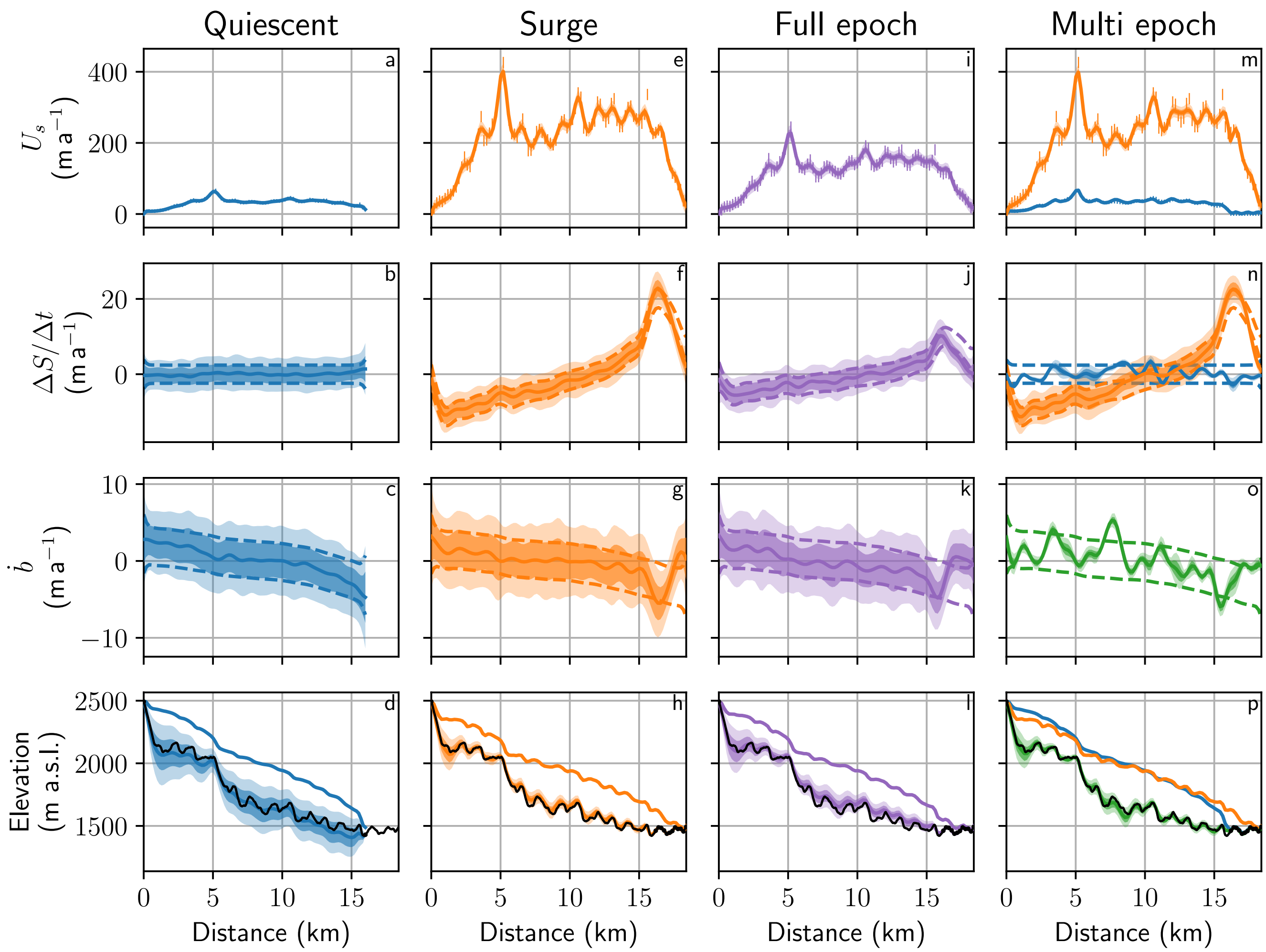

Fig. S8. Distributions of model variables for inversions with synthetic data: surface speed (row 1) with coloured vertical lines representing one standard deviation of observational uncertainty, surface-elevation change rate (row 2) with standard deviation of priors shown as dashed lines (mean omitted to reduce clutter), surface mass balance (row 3) with dashed lines as above, surface and bed elevation (row 4) shown along with true bed (black lines) and known bed elevations input to the model (black dots). In all panels, the posterior means and one and two standard deviations are shown in colour by solid line, dark shading and light shading, respectively. Posterior distributions are narrow where shading is not visible. (a)–(d) Quiescent regime (column 1). (e)–(h) Surge regime (column 2). (i)–(l) Full-epoch inversion (column 3). (m)–(p) Multi-epoch inversion (column 4).

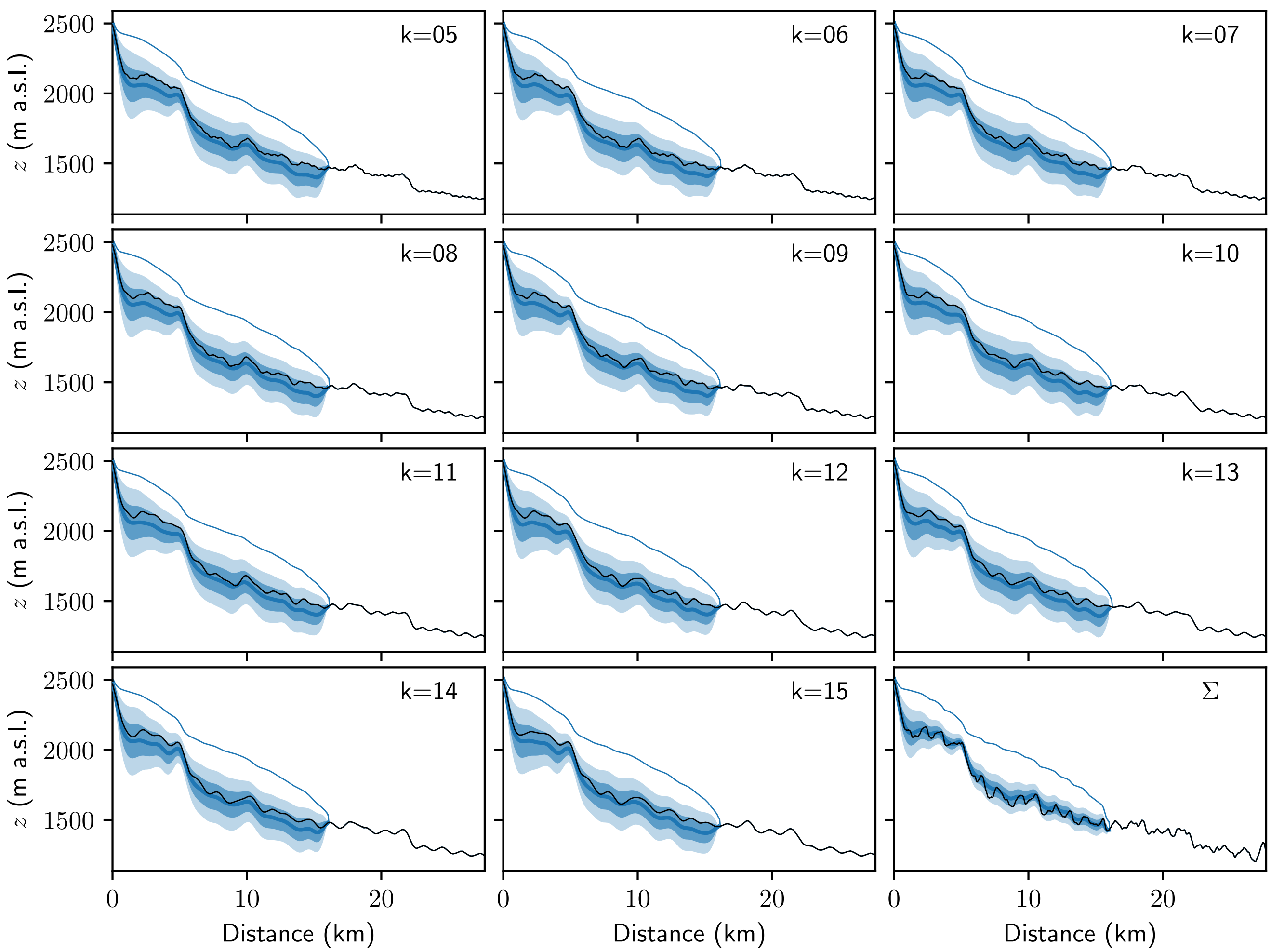

Fig. S9. Posterior distributions of the bed using data from deformation-only (quiescent) regimes for each synthetic profile (see Figure 4.1 and main text). In all panels, the posterior means and one and two standard deviations are shown in colour by solid lines, dark shading and light shading, respectively. True beds shown in black.

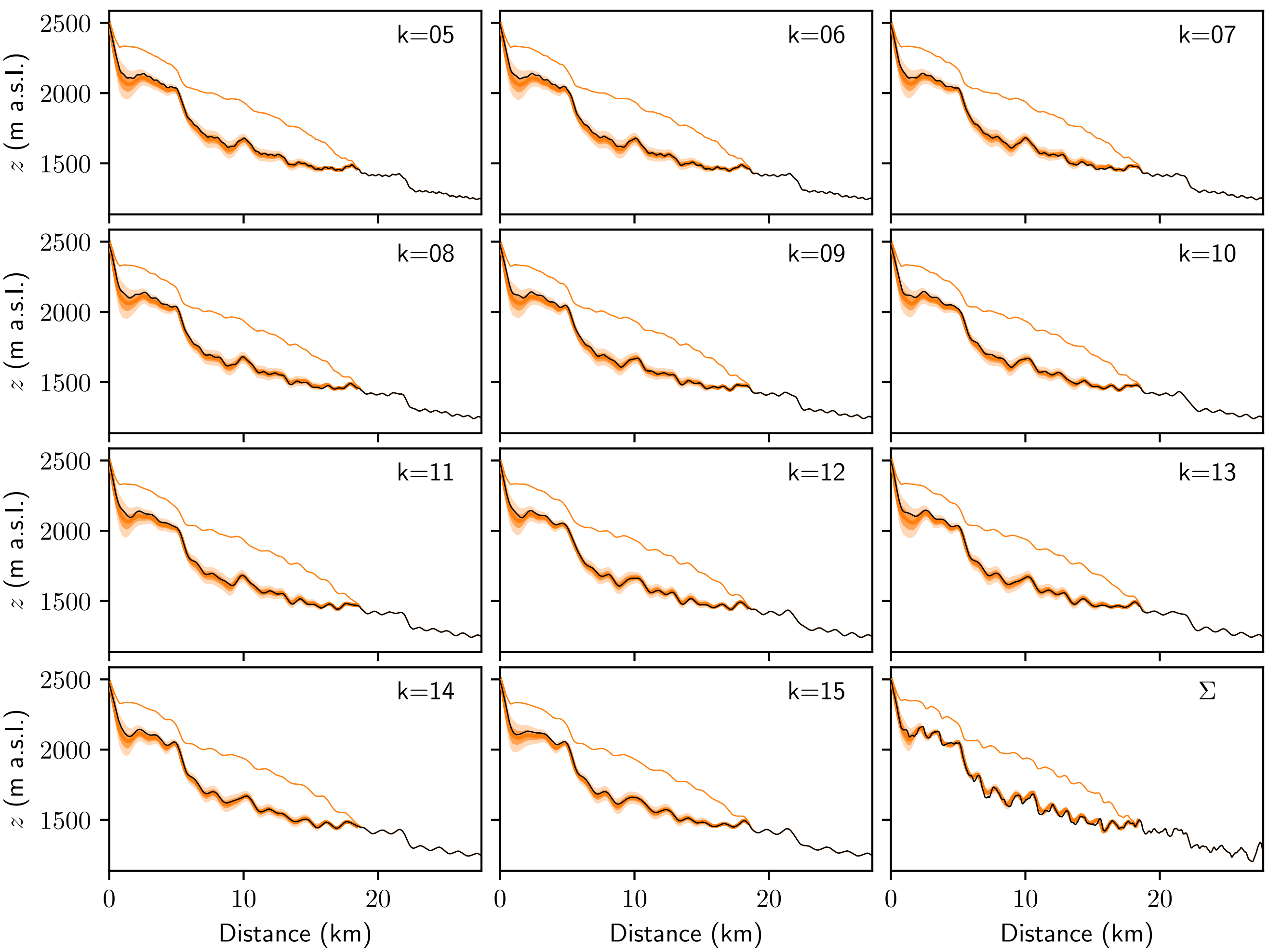

Fig. S10. Posterior distributions of the bed using data from high-slip (surge) regimes for each synthetic profile (see Figure 4.1 and main text). In all panels, the posterior means and one and two standard deviations are shown in colour by solid lines, dark shading and light shading, respectively. True beds shown in black.

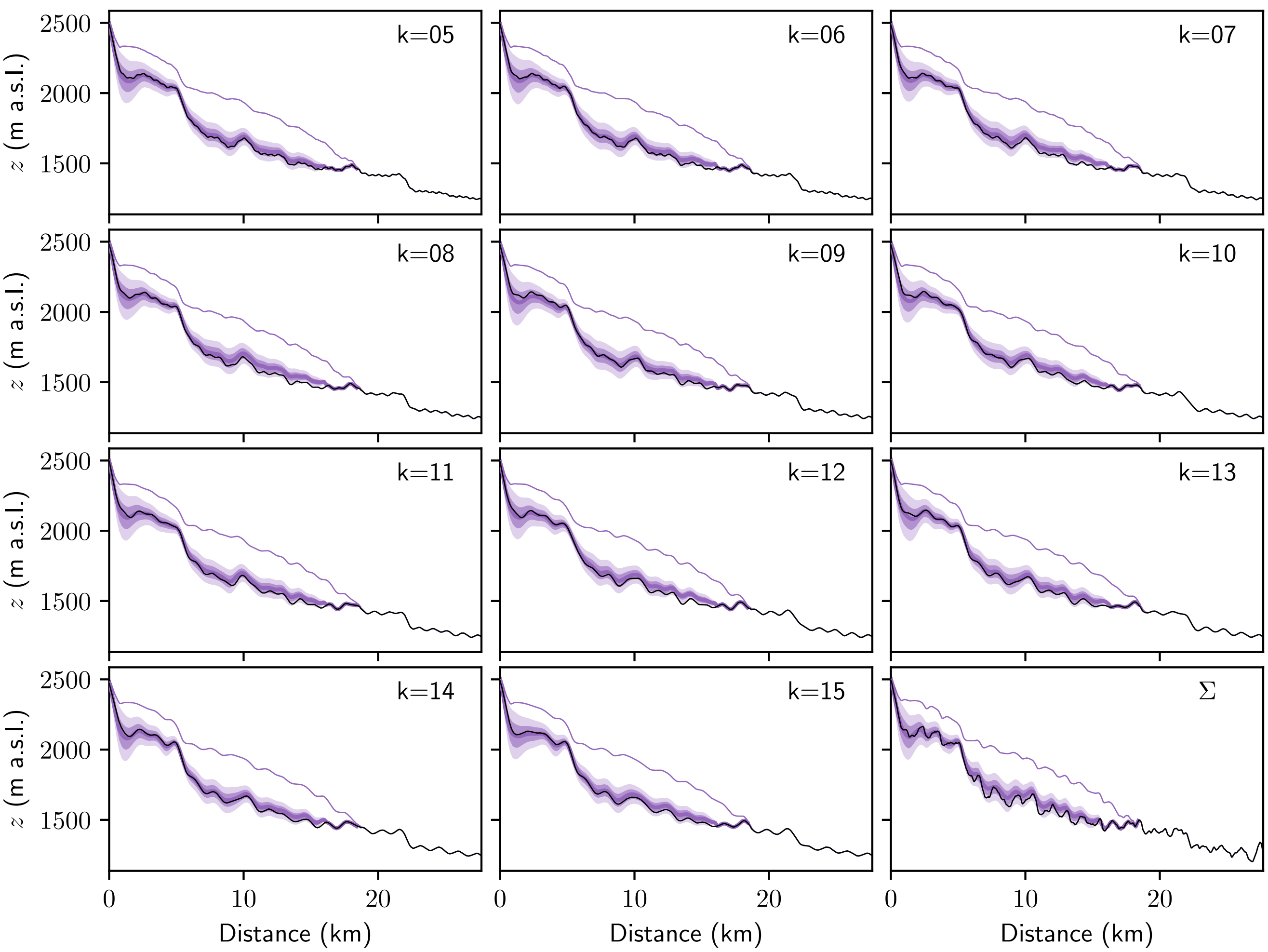

Fig. S11. Posterior distributions of the bed using full-epoch inversions for each synthetic profile (see Figure 4.1 and main text). In all panels, the posterior means and one and two standard deviations are shown in colour by solid lines, dark shading and light shading, respectively. True beds shown in black.

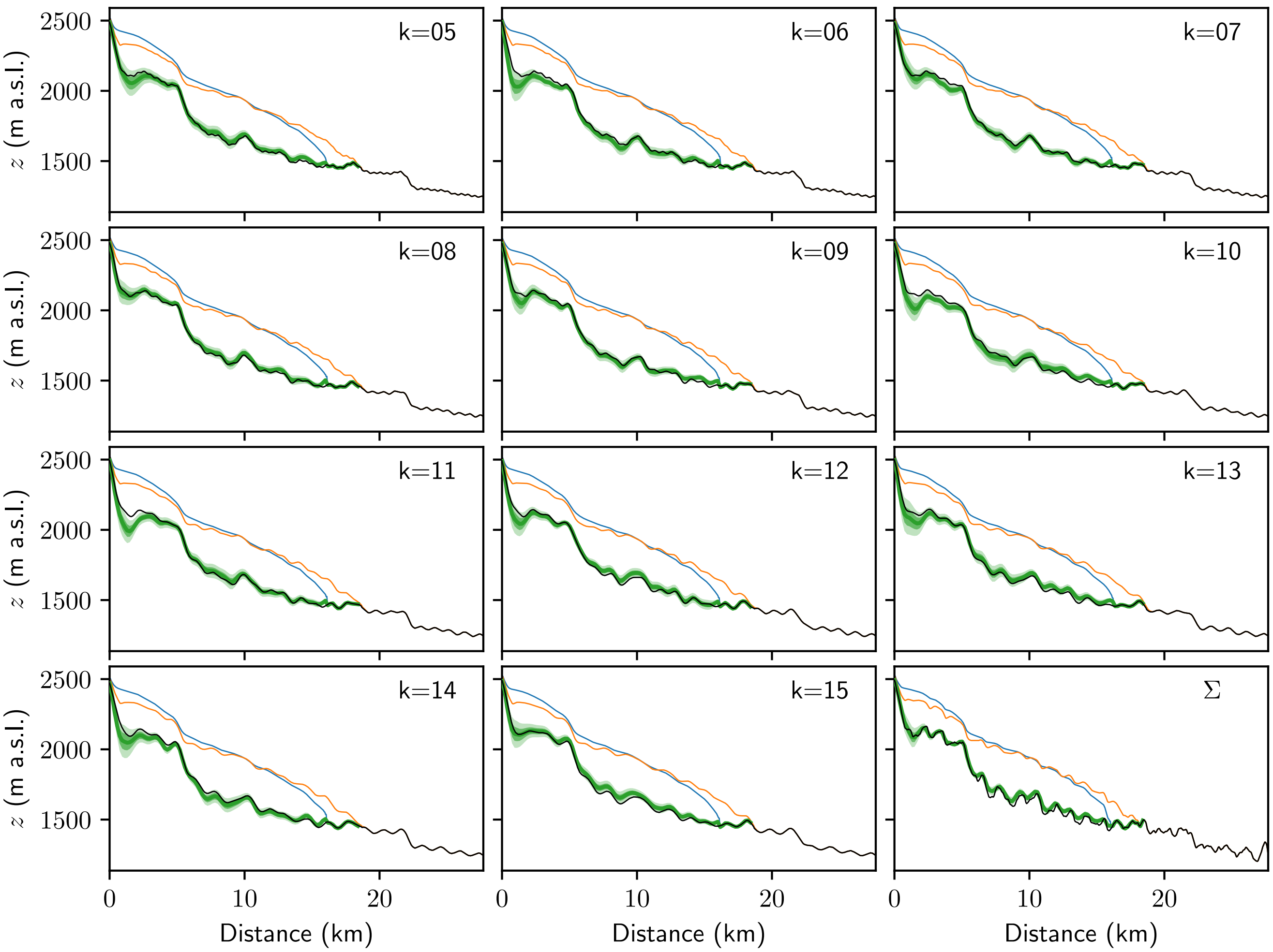

Fig. S12. Posterior distributions of the bed using multi-epoch inversions for each synthetic profile (see Figure 4.1 and main text). In all panels, the posterior means and one and two standard deviations are shown in colour by solid lines, dark shading and light shading, respectively. True beds shown in black.

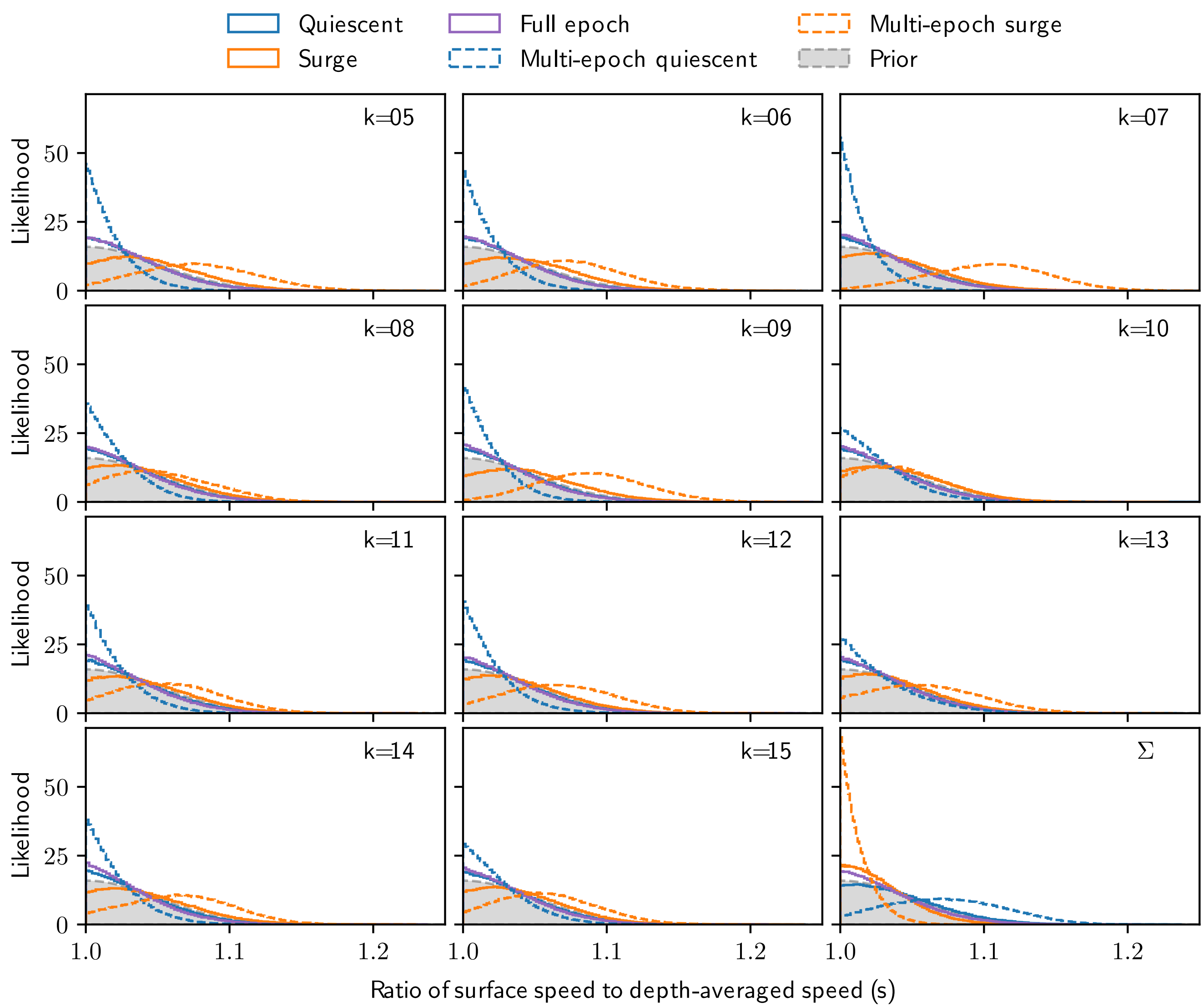

Fig. S13. Prior (gray shaded) and posterior (solid and dashed coloured lines) distributions of the ratio of surface to depth-averaged glacier flow speed (s) for each synthetic profile (see Figure 4.1 and main text). $s = 1.0$ represents plug flow (pure sliding).

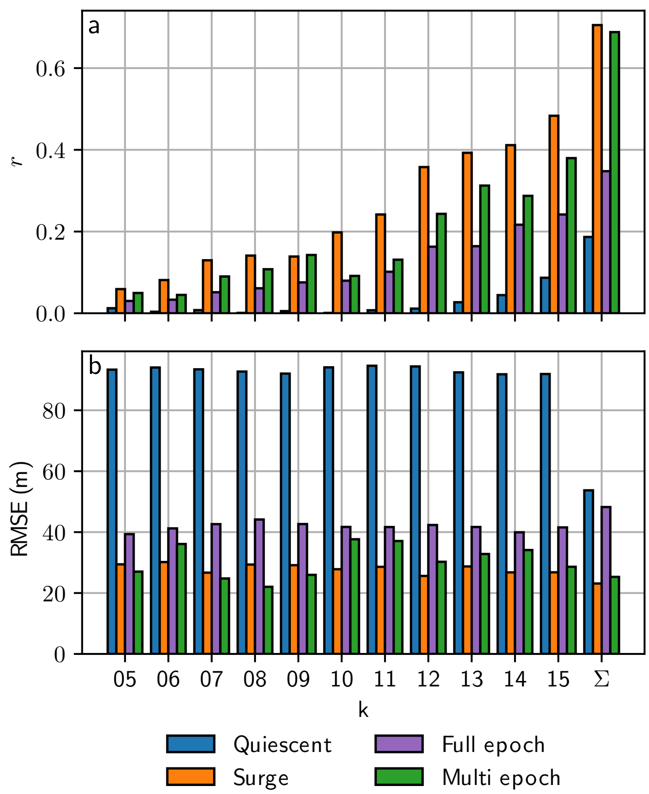

Fig. S14. Mean values of distributions of Pearson correlation coefficient r and Root Mean Square Error (RMSE) between the true and posterior beds for individual values of k as well as the composite bed (far right). Distributions were generated by computing r and RMSE between the true bed and each realization of the bed in the posterior distributions.

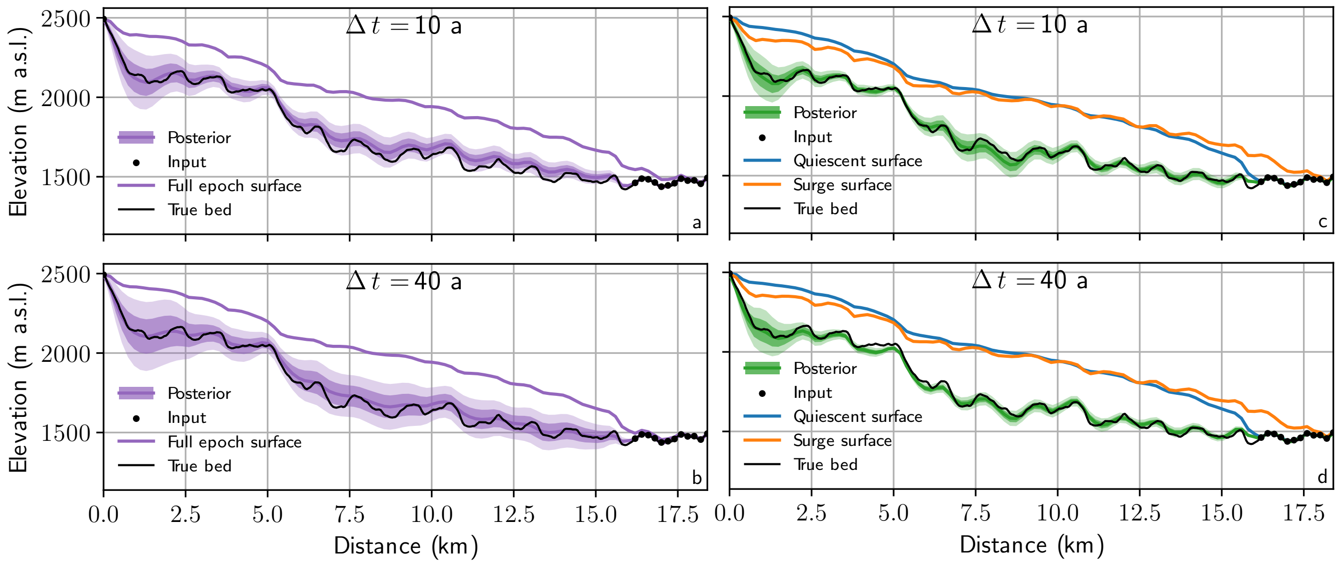

Fig. S15. Comparison of full-epoch and multi-epoch inversions of synthetic data for composite bed with two different prescribed quiescent intervals: 10 a (top row) and 40 a (bottom row). (a) Full-epoch inversion with 10 a quiescent period. (b) Full-epoch inversion with 40 a quiescent period. (c) Multi-epoch inversion with 10 a quiescent period. (d) Multi-epoch inversion with 40 a quiescent period.

values of k, and for the composite bed, mean values of r are highest for the high-slip (surge) regime, lowest for the deformation-only (quiescent) regime and intermediate for the multi-epoch and full-epoch inversions. Mean values of RMSE (Figure S14b) are roughly consistent across individual values of k. In most cases, inversions with data from the high-slip (surge) regime produce the lowest RMSEs, while those from the deformation-only (quiescent) regime produce the highest. The full-epoch and multi-epoch inversions lie in between, with the multi-epoch inversion out-performing the full-epoch inversion in every case.

4.2 Inversions of synthetic data with longer quiescent interval

The reference model in the main text assumed an arbitrary quiescent interval of 10 a. Inversion results for an assumed quiescent interval of 40 a are compared with those for 10 a in Figure S15. Inversions using quiescent-only and surge-only data (see main text) are unaffected by the prescribed quiescent interval, hence are not shown again here. Extending the quiescent interval from 10 a to 40 a results in loss of information in the full-epoch inversion, resulting in a smoother bed for the 40 a case (purple, Figures S15a,b). In contrast, the multi-epoch approach exhibits no loss of information in the 40 a case, with comparable bed posteriors (green, Figures S15c,d). This example demonstrates the increasing differential advantage of the multi-epoch over full-epoch approach as the quiescent interval increases.

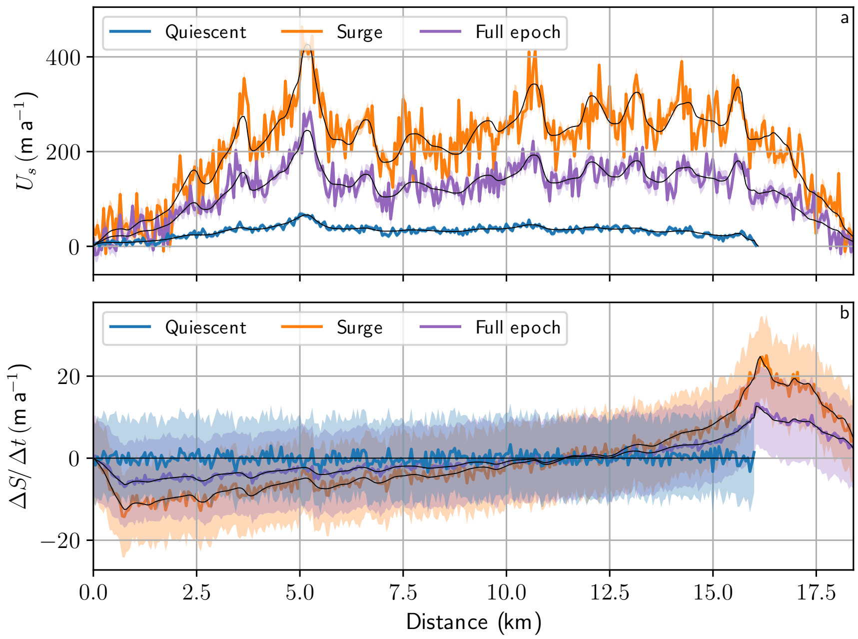

Fig. S16. Synthetic input data (solid coloured lines) for composite-bed inversions with added noise: deformation-only (quiescent) regime in blue, high-slip (surge) regime in orange and full epoch in purple (time-weighted average of blue and orange curves). Multi-epoch inversion uses data in blue and orange. Shading indicates one standard deviation intended to represent observational uncertainty. The noise-free data are shown with fine black lines for reference. (a) Surface speed. (b) Surface-elevation change rate.

4.3 Inversions of synthetic data with added noise

Figure S16 shows noisy synthetic surface speeds and elevation change rates derived from the original synthetic data with added random noise. The noise is assumed to be Gaussian with a standard deviation equal to 25% of the flowline-averaged magnitude of the individual surface speed or elevation change rate profiles. The mass-balance data remain unchanged. The corresponding inversion results (Figure S17) bear a qualitative similarity to the noise-free inversion results in the main text, including preservation of the relative performance of the four different inversions (surge, multi-epoch, full-epoch, quiescence).

5 DISTRIBUTIONS OF MODEL VARIABLES FOR REAL DATA

Figure S18 shows distributions of surface speed, elevation change rate, mass balance and surface/bed elevation for all four inversions of real data.

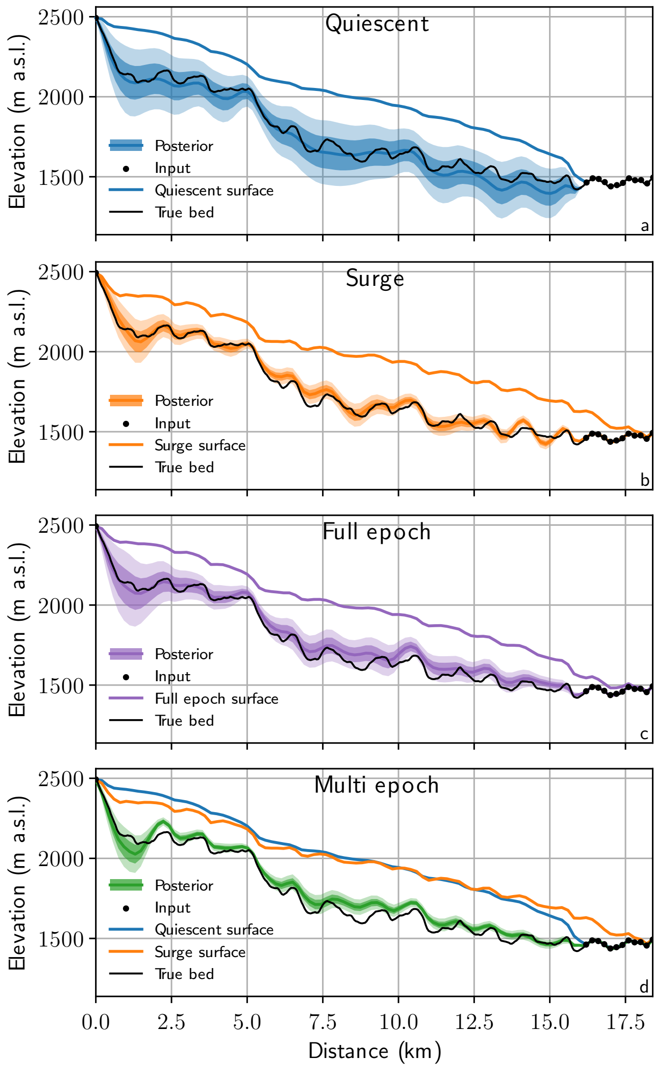

Fig. S17. Posterior distributions of the bed using noisy synthetic data (Figure S16). (a) Deformation-only (quiescent) regime. (b) High-slip (surge) regime. (c) Full-epoch inversion. (d) Multi-epoch inversion.

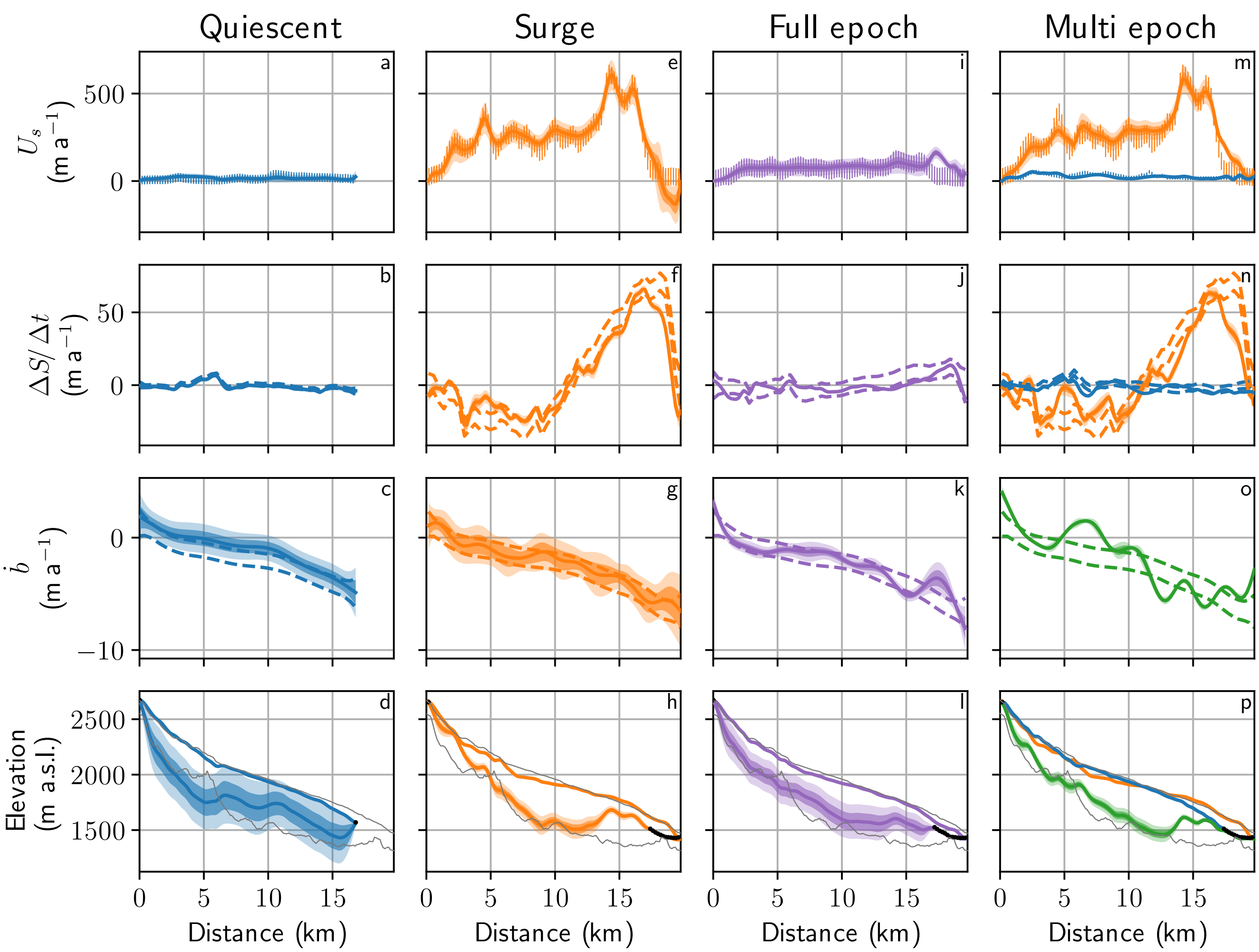

Fig. S18. Distributions of model variables for inversions with real data: surface speed (row 1) with coloured vertical lines representing one standard deviation of observational uncertainty, surface-elevation change rate (row 2) with standard deviation of priors shown as dashed lines (mean omitted to reduce clutter), surface mass balance (row 3) with dashed lines as above, surface and bed elevation (row 4) shown along with values from Farinotti and others (2019) (fine grey lines) and known bed elevations input to the model (black dots). In all panels, the posterior means and one and two standard deviations are shown in colour by solid line, dark shading and light shading, respectively. Posterior distributions are narrow where shading is not visible. (a)–(d) Quiescent regime, 2007–2016 (column 1). (e)–(h) surge regime, 2016–2018 (column 2). (i)–(l) Full-epoch inversion, 2007–2018 (column 3). (m)–(p) Multi-epoch inversion, 2007–2016 and 2016–2018 (column 4).

REFERENCES

Berthier E, Schiefer E, Clarke GKC, Menounos B and Rémy F (2010) Contribution of Alaskan glaciers to sea-level rise derived from satellite imagery. *Nature Geoscience*, **3**(2), 92–95, ISSN 1752-0894, 1752-0908 (doi: 10.1038/ngeo737)

Brinkerhoff DJ, Aschwanden A and Truffer M (2016) Bayesian inference of subglacial topography using mass conservation. *Frontiers in Earth Science*, **4**, 1–15 (doi: 10.3389/feart.2016.00008)

Consortium R (2017) Randolph glacier inventory – a dataset of global glacier outlines: Version 6.0: Technical report, global land ice measurements from space, colorado, usa. digital media. (doi: https://doi.org/10.7265/N5-RGI-60)

Farinotti D, Huss M, Fürst JJ, Landmann J, Machguth H, Maussion F and Pandit A (2019) A consensus estimate for the ice thickness distribution of all glaciers on Earth. *Nature Geoscience*, **12**(3), 168–173 (doi: 10.1038/s41561-019-0300-3)

Farr TG, Rosen PA, Caro E, Crippen R, Duren R, Hensley S, Kobrick M, Paller M, Rodriguez E, Roth L and others (2007) The shuttle radar topography mission. *Reviews of Geophysics*, **45**(2) (doi: 10.1029/2005RG000183)

Fonnesbeck C, Patil A, Huard D and Salvatier J (2015) Pymc: Bayesian stochastic modelling in python. *Astrophysics Source Code Library*, ascl–1506

Gagliardini O, Zwinger T, Gillet-Chaulet F, Durand G, Favier L, de Fleurian B, Greve R, Malinen M, Martín C, Råback P, Ruokolainen J, Sacchettini M, Schäfer M, Seddik H and Thies J (2013) Capabilities and performance of Elmer/Ice, a new-generation ice sheet model. *Geoscientific Model Development*, **6**(4), 1299–1318 (doi: 10.5194/gmd-6-1299-2013)

Gelman A, Carlin JB, Stern HS and Rubin DB (1995) *Bayesian Data Analysis*. Chapman and Hall/CRC

Hock R (1999) A distributed temperature-index ice-and snowmelt model including potential direct solar radiation. *Journal of Glaciology*, **45**(149), 101–111 (doi: 10.1017/S0022143000003087)

Maussion F, Butenko A, Champollion N, Dusch M, Eis J, Fourteau K, Gregor P, Jarosch AH, Landmann J, Oesterle F and others (2019) The open global glacier model (OGGM) v1.1. *Geoscientific Model Development*, **12**(3), 909–931 (doi: 10.5194/gmd-12-909-2019)

Nye J (1965) The flow of a glacier in a channel of rectangular, elliptic or parabolic cross-section. *Journal of Glaciology*, **5**(41), 661–690 (doi: 10.3189/S0022143000018670)

Pedregosa F, Varoquaux G, Gramfort A, Michel V, Thirion B, Grisel O, Blondel M, Prettenhofer P, Weiss R, Dubourg V, Vanderplas J, Passos A, Cournapeau D, Brucher M, Perrot M and Duchesnay E (2011) Scikit-learn: Machine learning in Python. *Journal of Machine Learning Research*, **12**, 2825–2830

Young EM, Flowers GE, Berthier E and Latto R (2021) An imbalancing act: the delayed dynamic response of the Kaskawulsh Glacier to sustained mass loss. *Journal of Glaciology*, **67**(262), 313–330 (doi: 10.1017/jog.2020.107)